Article:
Metilli, L, Storm, M, Bodey, AJ et al. (5 more authors) (2021) Investigating the microstructure of soft, microporous matter with synchrotron X-ray tomography. Materials Characterization, 180. 111408. ISSN 1044-5803

https://doi.org/10.1016/j.matchar.2021.111408

Investigating the microstructure of soft, microporous matter with synchrotron X-ray Tomography

Lorenzo Metilli[1], Malte Storm[2], Andrew J. Bodey[2], Kaz Wanelik[2], Arwen I.I. Tyler[1], Aris Lazidis[3], Stephanie Marty-Terrade[4], Elena Simone[1]*

[1] *School of Food Science and Nutrition, Food Colloids and Bioprocessing Group, University of Leeds, Leeds, LS29JT, United Kingdom*

[2] *Diamond Light Source Ltd., Harwell Science and Innovation Campus, Didcot, OX 11 0DE, United Kingdom*

[3] *Nestlé Product Technology Centre Confectionery York, Haxby Road, York YO31 8TA, United Kingdom*

[4] *Nestlé Research, Vers-chez-les-Blanc, 1000 Lausanne 26, Switzerland*

**Corresponding author: e.simone@leeds.ac.uk*

Abstract

Soft porous matter is commonly encountered in artificial tissue applications, pharmaceuticals delivery systems and in cosmetic and food products. These materials are typically opaque and tend to deform under very small levels of shear; this makes the characterization of their microstructure very challenging, particularly in the native state. Air-in-oil systems (oleofoams) are an emerging type of soft material with promising applications in cosmetics and foods, which contain air bubbles stabilized by Pickering fat crystals dispersed in a liquid oil phase. Synchrotron radiation X-ray computed tomography (SR - XCT) is a non-invasive, non-destructive technique increasingly used to investigate multiphasic, porous materials, owing to its high flux which enables sub-micron resolution and significant statistics at rapid acquisition speed. While the

penetration of high energy X-rays can provide high resolution images and allows the reconstruction of the 3D structure of samples, the experimental setup and measuring parameters need to be carefully designed to avoid sample deformation or beam damage.

In this work, a robust methodology for investigating the 3D microstructure of soft, porous matter was developed. Sample preparation and experimental setup were chosen to allow synchrotron tomographic analysis of soft oleofoams with a low melting point (<30°C). In particular, the use of cryogenic conditions (plunge-freeze in liquid nitrogen) provided stability against melting during the acquisition. Additionally, an image processing workflow was designed for analysing the 3D microstructure of the samples using ImageJ. Hence, the size and shape distribution of the air phase, as well as the thickness of the continuous gel phase could be determined for samples with significantly different microstructures (fresh vs. heated). Furthermore, the use of time-resolved X-ray radiography (XRR) allowed to study dynamic changes in the microstructure of the samples during thermal destabilization, visualizing bubble coalescence and growth in optically opaque foam samples with a sub-second timescale.

Introduction

Soft porous matter features in numerous contexts of scientific and commercial interests, ranging from hydrogel-based scaffold for tissue regeneration (Sato et al., 2018; Kinoshita et al., 2020), porous nanocellulose for delivery of pharmaceuticals (Sehaqui et al., 2010; Iftimi et al., 2019) gas marbles (Timounay et al., 2017) to aqueous and non-aqueous foams used in food and personal care products (Fameau & Fujii, 2020; Hill & Eastoe, 2017; Luengo et al., 2021). These systems are comprised of a dispersed gaseous phase, a liquid or semi-solid continuous phase and, in the case of foams, suspended stabilizing molecules, particles or crystals that can also adsorb at the air phase boundary (Murray et al., 2011; Murray, 2020). The 3D microstructure dictates the macroscopic properties of these materials, which in turn affects their functionality, their stability against liquid drainage and liquid coalescence and, in the case of food, texture and mouthfeel (Ciurzyńska & Lenart, 2016; Ellis et al., 2017; Herremans et al., 2013) Furthermore, the relationship between raw ingredients, processing conditions and resulting microstructure in porous matter

is complex and still not fully understood. Nevertheless, it is extremely important for the design of novel products with tuned properties, that new techniques and methodologies which clarify such relationship to be developed (Lazidis et al., 2017).

Investigating the microstructure of soft porous matter is a challenging task, as these materials are usually optically opaque, prone to deformation and often subject to melting at room temperatures (Ubbink et al., 2008; Murray et al., 2011). Standard optical microscopy is a readily available and commonplace technique for characterization of materials; however, sample preparation is intrusive, as it requires the sample to be placed between two glass covers, which can affect significantly the native structure of the specimen (Metilli et al., 2020) and consequently, the measured bubble size and shape distribution. Furthermore, most microscopy techniques provide only 2D, surface information on the sample microstructure, limiting the accuracy of the measurement. Even confocal microscopy, which can probe the sample along the z-axis, suffers from a limited field of view and accessible depth range, which hinders the collection of statistically significant 3D data of macroscopic samples.

X-ray computed tomography (XCT) has been increasingly used to analyse the microstructure of soft and porous materials, owing to its non-invasive and non-destructive approach (Barigou & Douaire, 2013). Soft biological matter is usually weakly-absorbing with respect to X-rays, and hence a contrast agent may be added during sample preparation to stain the continuous phase. Contrast agents such as sodium iodide (NaI) increase the absorption of X-rays, which improves the contrast of different phases during acquisition. However, the addition of the contrast agent might cause either excessive absorption of X-rays by the sample, or alter its properties prior to imaging. The image contrast can also be enhanced using phase-contrast imaging (PCI), which measures the X-ray refractivity in the sample, rather than the attenuation (Wang et al., 2018). Benchtop XCT instruments are becoming increasing accessible; however, they require lengthy acquisition times, which make this technique unsuitable for temperature sensitive (*e.g.*, low melting point) or delicate samples, as prolonged beam exposure can cause heating, X-ray radiation damage and deformation in the microstructure due to sample movement (Wang et al., 2018). Synchrotron radiation XCT (SR-XCT), on the other hand, provides high flux X-ray sources with short exposure times and high signal-to-

noise ratio, reducing significantly the length of the experiment, as well as sub-micron voxel resolution. Customizable sample environments, such as temperature and humidity control, and application of shear on the sample allow dynamic microstructural investigation of specimens when subject to external stimuli (Rau et al., 2017).

Bread dough can be considered a model soft porous material of great industrial relevance, in which the microstructure is intimately linked to its rheology profile and ultimately taste perception (Jekle & Becker, 2011). Wheat flour dough displays relatively high viscosity, no creaming of air bubbles and good tolerance to X-ray exposure, without requiring carefully designed imaging protocols. Early work reported by Babin and colleagues demonstrated the efficacy of synchrotron XCT in characterizing the microstructure of bread dough during its processing steps (*i.e.* proofing and baking) with a spatial resolution of 15 µm (Babin et al., 2006). Owing to the ability to track individual bubbles in the sample, the authors were able to model the growth of gas cells developing in the dough, as well as their coalescence during proofing. The spatial resolution of the instruments was a critical parameter in the detection of smaller air bubbles, as reported by more recent publications by Trinh et al. (2013) and Koksel et al. (2016). Here the smaller voxel size (*ca.* 10 and 8.75 µm, respectively) of the instrument resulted in a ten-fold increase in the bubble density detected in dough samples compared with previous works; this allowed a more accurate description of the gas phase evolution during dough mixing (Trinh et al., 2013) and of the time-dependent bubble disproportionation in non-yeasted samples (Koksel et al., 2016). Sample density calculated from gravimetric methods is routinely used to validate XCT results in these works (Campbell et al., 2001).

In the case of soft porous materials with higher susceptibility to shear and melting, additional steps are required during sample preparation and characterization. Ice cream is a complex multiphasic porous material made of a dispersed gas phase, ice crystals, and a continuous aqueous phase. The complex interplay between its ingredients and phases – which is still not fully understood – is crucial in ensuring high quality products and for the design of novel ice cream formulations (Bahram-Parvar, 2015). Over the last decade, XCT has been increasingly used to characterize ice cream. Pinzer et al. (2012) used a benchtop XCT scanner to investigate the microstructure of ice cream and its evolution upon thermal cycling. The instrument had a

nominal 6 µm voxel resolution, and sodium iodide was added to the ice cream recipe to enhance contrast between the air and the ice crystals. To successfully segment the three main phases from the tomography images, the authors developed an edge-preserving smoothing filter, based on the anisotropic diffusion algorithm. The segmentation was then validated using the calculated ice fraction of the sample from differential scanning calorimetry measurements.

A similar method was applied more recently on frozen sorbets by Masselot et al. (2021), using a 3D-printed cold stage to keep a low sample temperature during the measurements. The voxel resolution of the scanner used was 9 microns. This study focused mostly on measuring the size distribution of the air bubbles and the ice crystals; CryoSEM was used to validate the XCT measurements and the two techniques showed values of the same order of magnitude and similar range. In both this work and that of Pinzer et al. (2012), however, the scanning time for one sample was between 10 and 15 minutes, which might not be suitable for other types of soft porous materials that are particularly susceptible to X-ray damage. Furthermore, the authors acknowledged that, due to low spatial resolution, air bubbles smaller than 20 – 15 microns were not measured.

These limitations were overcome by the use of a synchrotron source, as presented by Guo and co-workers in a series of recent publications (Guo et al., 2017; Guo et al., 2018; Mo et al., 2018). Here the authors focused on the characterization of ice cream microstructure using SR-XCT, with a nominal voxel resolution of 0.8 µm and fast acquisition times (in the order of minutes). The sample was initially maintained at low temperatures (- 15°C). To improve further the segmentation of the different phases in ice cream – air, ice crystals and unfrozen matrix – a novel computational approach was developed to reduce noise and improve intensity homogeneity in the different phases. The effects of thermal cycling on individual air cells and ice crystals and on the unfrozen matrix were investigated using a bespoke temperature-controlled stage and short acquisition times for tomography scans (~ 2.5 minutes each). Nevertheless, there are still destabilization mechanisms in soft matter that occur on shorter time scales than minutes (*i.e.,* seconds or milliseconds), such as droplet or bubble coalescence, Ostwald ripening or disproportionation, or liquid film rupturing, which require suitable time-resolved techniques to be captured and investigated.

Despite these recent advances in the use of SR-XCT in soft porous materials, at present many relevant materials are still missing a suitable three-dimensional, close-to-native state methodology for the characterization of their microstructure and its dynamics of destabilisation. Moreover, in light of the current trends of products reformulation with more sustainable and biocompatible ingredients, soft material characterization is of paramount importance (Cornwell, 2018; Manzocco et al., 2021; McClements, 2020). Personal care products such as shampoos, which are surfactant-stabilized aqueous foams, owe their consumer appeal to their foamability and foam stability (Luengo et al., 2021); yet a description of their aerated microstructure is currently lacking. Similarly, the fire suppression dynamics of firefighting foams are highly correlated with their bubble size distribution and coarsening, which would benefit from a suitable 3D characterization (Kennedy et al., 2015). Low-viscosity samples prone to movement may benefit from the use of ultra-fast tomography techniques, which enable total acquisition times close to the second (Dittmann et al., 2016).

Recently, air-in-oil systems have received significant attention due to their untapped potential in the field of low-fat food products, oil-based cosmetics and pharmaceutical delivery systems (Heymans et al., 2017; Fameau & Binks, 2021). Air-in-oil systems, also called oleofoams, consist of a continuous liquid oil phase in which gas bubbles are stabilized by fat crystals. These materials exhibit a melting range close to body temperature, they deform under small levels of shear and are subject to destabilization mechanisms such as oil drainage and bubble coalescence (Heymans et al., 2018; Saha et al., 2020; Truong et al., 2019). For these reasons the analysis of their microstructure is very challenging. While several studies have focused on the relationship between crystal properties and resulting microstructure, the characterization of these materials is usually carried out using optical or confocal microscopy. Up to the present, the native, three-dimensional arrangement of the air bubbles in oleofoams has not been investigated due to the lack of suitable techniques and methods to obtain meaningful parameters describing the microstructure.

In this paper, a novel methodology is proposed, which aims at investigating the microstructure of delicate soft porous matter in a non-invasive fashion (*i.e.,* without the use of contrast agents), with a straightforward cryogenic procedure to prevent deformation in the sample caused by melting, stage rotation or beam

damage. The method was demonstrated using cocoa butter-based oleofoams recently characterized in a previous publication (Metilli et al., 2021). The effect of temperature on the microstructure of the specimens was studied using SR-XCT and X-ray Radiography (SR-XRR), to track fast dynamic changes in the sample during heating or cooling. The methodology presented in this work enables the extraction of several microstructure descriptors, including the air volume fraction and its distribution within the sample, the size and shape distribution of the gas phase and the thickness of the continuous phase. Furthermore, SR-XRR was also used to dynamically monitor changes in the air phase heating of samples. While this method was demonstrated with edible oleofoams, it is applicable to the analysis of similar types of sensitive, soft porous materials.

Materials and Methods

Sample preparation

The oleofoams investigated in this paper have been described and characterized in a previous publication (Metilli et al., 2021). Briefly, mixtures of cocoa butter (CB) and high oleic sunflower oil in different weight ratios were crystallized under shear in a lab-scale vessel to obtain an oleogel. For this work the samples were obtained using two crystallization conditions: (1) samples containing 15% w/w CB and crystallized at a -0.10 °C/min nominal cooling rate (sample named "15S") and (2) samples containing 30% w/w CB and crystallized at -0.75 °C/min (sample named "30F"). The oleogel was then aerated using a kitchen mixer in cycles of 5 minutes whipping and 10 minutes resting, for a total whipping time of 30 minutes. The whipping temperature was monitored during aeration and increased between 7 °C and 20 °C. In order to measure the air incorporation, during the rest step the sample was weighed in triplicates using a cup of fixed volume (30 mL). To ensure proper filling of the cup, the sample was added stepwise and set through percussion of the cup. The oleofoam overrun (related to air incorporation) was calculated using Equation 1:

$$Overrun\ (\%) = \frac{(w_{oleogel} - w_{oleofoam})}{w_{oleofoam}} \times 100 \qquad \text{Eq. 1}$$

where $w_{oleogel}$ and $w_{oleofoam}$ are the weight of the un-whipped oleogel and the weight of the oleofoam, respectively. To calculate the overrun from the tomography data, the following equation was used (Equation 2):

$$Overrun\ (\%) = \frac{\varphi_{air}}{1 - \varphi_{air}} \times 100 \qquad \text{Eq. 2}$$

where ϕ_{air} is the air volume fraction of the measured Volume of Interest (VOI) of each sample. In this work, both oleofoam samples 15S and 30F were analysed with X-ray Tomography after 5 minutes of aeration and at the end of the aeration step. The overrun measured with the cup method was compared with the overrun calculated from the X-ray Tomography data. To verify any statistically significant difference between the two datasets, a t-test with a *p*-value of 0.05 was performed. The analysis was carried out on two repetitions.

Beamline setup

The experiments were carried out at beamline I13-2, Diamond Light Source (Didcot, UK), using a pink beam source with a mean energy of 27 keV ($\sigma_E = 5\ keV$).The 2D projections for tomography and radiography were acquired with a PCO edge 5.5 CMOS camera (2560 x 2160 pixels). The total optical magnification was set to 8x, with an effective pixel size of 0.8125 µm. A small amount (*ca.* 1 mm^3) of oleofoam sample was then gently mounted on the top of a cut toothpick, minimizing deformation prior to the analysis. The toothpick was then glued to a cryocap, and mounted on the tomography stage. A cryo-jet (Cryojet XL, Oxford Instruments, UK) was installed to allow cooling and heating of samples on the beamline. A schematic of the experimental setup is provided in Figure 1.

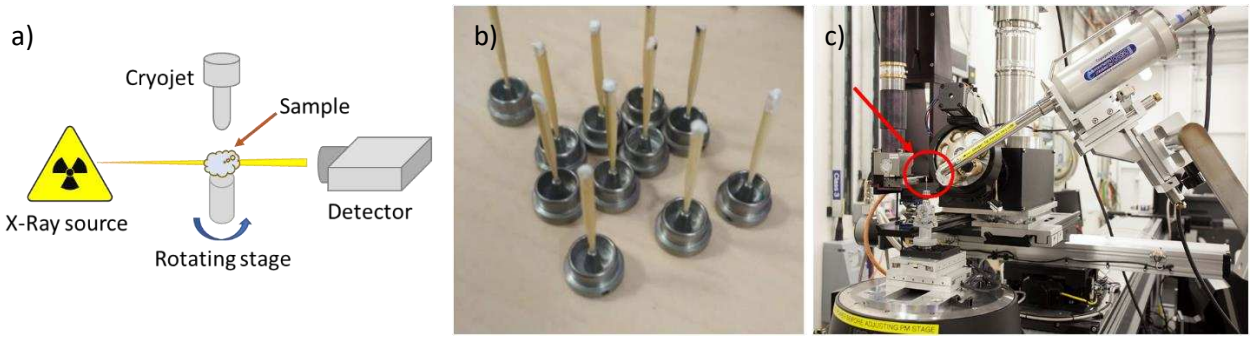

Figure 1. Schematic of the tomography setup (a), oleofoam samples on cut toothpicks (b) and sample mounted on the rotational stage with the Cryojet temperature control.

Two experimental protocols were tested: in the first, samples were mounted on the rotational stage and imaged directly at room temperature without temperature control, with an exposure time of 10 ms and for a total acquisition time of 20 seconds. The second protocol involved flash-freezing samples by immersion in liquid nitrogen (-196 °C) prior to imaging and controlling their temperature during scanning using a cryogenic nitrogen jet (Figure 1c). The Cryojet temperature was set to -40°C, which allowed sample handling without the need of using cryogenic gloves. The exposure time for each X-ray projection was set to 100 ms, for a total acquisition time of 5 minutes. For both experimental protocols, the number of projections was set to 1001, from an optimization range between 2000 and 500, while the optimal propagation distance was empirically determined and found to be 80 mm.

Synchrotron X-ray Radiography of heated samples

Selected oleofoam samples were subjected to controlled heating using the Cryojet. The evolution of their microstructure was monitored using SR-XRR. The temperature profile was set as follows: equilibration at 293 K for 1 min, heating from 293 K to 300 K at 1 K/min, hold at 300 K for 5 minutes, and finally cooling from 300 K to 273 K at -6 K/min. The samples were imaged with X-ray Tomography before and after the thermal treatment. Around 1500 2D radiographies of the oleofoam samples were collected during the heating profile, with the aim of tracking dynamic changes in the microstructure due to temperature. The frames were collected every 0.677 seconds. The radiography images were normalized with respect to the camera *background* (dark field images) and the beam intensity distribution (flat field images), according to Equation 3:

$$I_{norm} = \frac{I_{raw} - I_{dark}}{I_{flat} - I_{dark}} \qquad \text{Eq. 3}$$

where I_{norm} is the normalized pixel intensity of the image, I_{raw} is the pixel intensity of the sample image (projection) and I_{dark} and I_{flat} are averaged pixel intensities of 20 dark field and 20 flat field images, respectively. Due to the superimposition of bubbles in the 2D projection, a stack of difference images was produced by subtracting the pixel values between the *i*-th and the *i+1*-th frame, in order to visualize changes

in the microstructure. The outline of the bubbles in the difference images was detected using the Image Processing Toolbox in MATLAB (Mathworks, USA), and the equivalent diameter and circularity of 10 bubbles was measured and compared with the 3D data obtained from X-ray Tomography.

To quantify the extent of microstructural changes in the sample during thermal treatment, the difference image stack was further analysed with Principal Component Analysis (PCA) in MATLAB (Mathworks, USA), using the *pca* function. The choice of PCA was justified due its ability to reduce redundancy in large datasets, and to detect changes in image sequences in an unsupervised fashion (Hussain et al., 2013; Celik, 2009), as bubble segmentation from the 2D difference images proved challenging to automate for analysis.

Reconstruction and Image post-processing

The 2D projections were reconstructed into a tomography volume using the Savu processing pipeline (Wadeson & Basham, 2016) using the gridrec algorithm in TomoPy (Gürsoy et al., 2014). The reconstruction pipeline included the following steps: image normalization using dark and flat field images, correction of the ring artefacts (Vo et al., 2018) and a Paganin filter, which is used to restore the phase information generated by the inline phase contrast (Paganin et al., 2002). Finally, the reconstructed volume was obtained using the *Gridrec* reconstruction algorithm in the TomoPy software package (Dowd et al., 1999).

Image post-processing was applied to the reconstructed tomography volumes to obtain quantitative parameters describing the air phase and the continuous phase of oleofoams. To facilitate the computation burden, each tomography volume was divided into a number of Volumes of Interest (VOI) of approximately 500x500x500 μm^3. A minimum of 5 randomly selected VOI were analysed and averaged for each sample. The stack of tomographic slices were processed using ImageJ 1.53 (National Institute of Health, USA) according to the following workflow: 3D median filtering, Otsu thresholding, 3D-Euclidean Distance Map Watershed (Legland et al., 2016).

241 The air cells were counted and measured using the BoneJ plugin for ImageJ (Doube et al., 2010) and excluding
242 the objects on the edges of the VOI. The volume and surface areas were used to compute the equivalent
243 diameter (D_{eq}) and the sphericity (Φ) of each air cell, according to the following equations (Eq. 4 and Eq. 5)

$$D_{eq} = \sqrt[3]{\frac{6V}{\pi}} \quad \text{Eq. 4}$$

$$\Phi = \frac{\pi^{\frac{1}{3}}(6V)^{\frac{2}{3}}}{A} \quad \text{Eq. 5}$$

244 D_{eq} was used to calculate the volume-weighted diameter (D[4,3]) of the air cells for a specific sample, using
245 Eq. 6

$$D[4,3] = \frac{\sum_{i=1}^{N} D_{eq} i^4}{\sum_{i=1}^{N} D_{eq} i^3} \quad \text{Eq. 6}$$

246 Moreover, the BoneJ plugin measured the major, intermediate and minor axis (a ≥ b ≥ c, respectively) of each
247 air bubble, which were used to calculate two aspect ratios: the Elongation Index (EI = b/a) and the Flat Index
248 (FI = c/b). By plotting EI against FI, four shape classes were described: spheroids, oblate, prolate and blade
249 (Blott & Pye, 2008; Zhao & Wang, 2016), and the number of air bubbles belonging to each shape class
250 counted. Finally, BoneJ was also used to calculate the air volume fraction and overrun of each VOI, according
251 to Eq. 2. The thickness of the oleogel phase (*i.e.* the continuous phase) was also calculated using the same
252 plugin, following the method described by Hildebrand & Rüegsegger (1997). The algorithm works by
253 inscribing spheres of maximal volume into the continuous phase structure and assigning each voxel the
254 diameter of the largest sphere it belongs to (Pinzer et al., 2012). In this publication, the distribution of the
255 assigned voxels for each sample is represented, alongside with the volume-weighted average thickness value.
256

Results and Discussion

Comparison of different imaging techniques

A comparison of different microscopy techniques for investigating the microstructure of oleofoams is presented in Figure 2, using a 30F oleofoam as a sample.

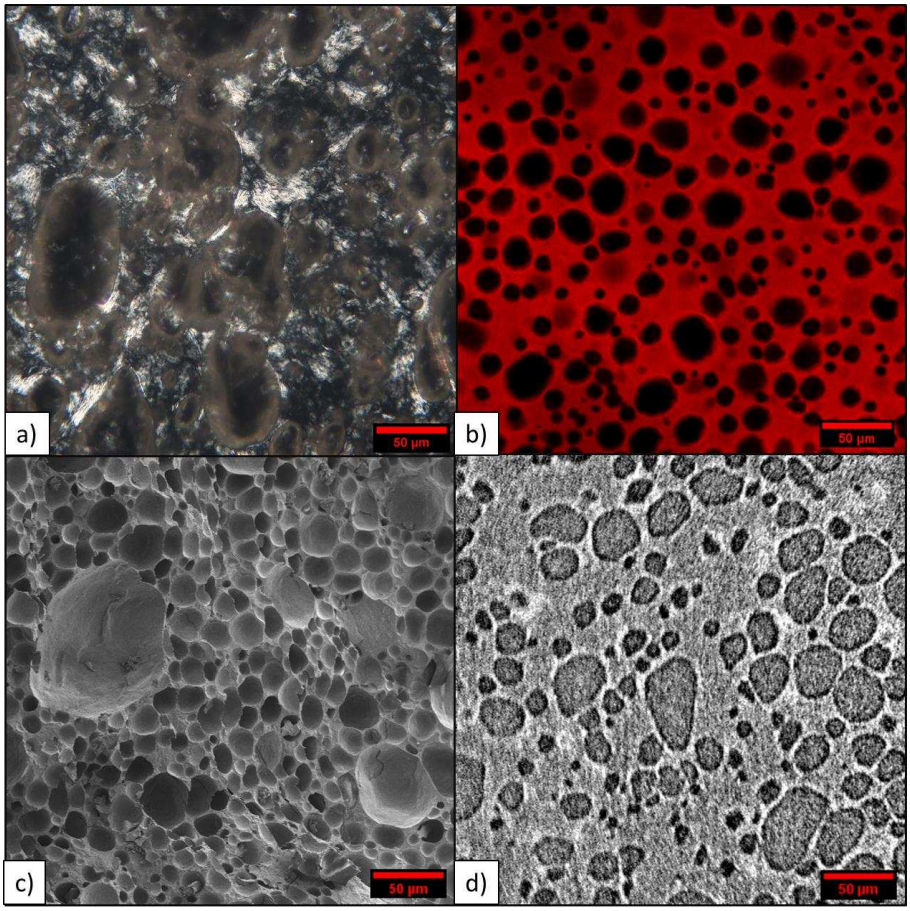

Figure 2. Comparison of microscopy techniques for the characterization of the microstructure of oleofoams. Polarized light microscopy (a) confocal microscopy (b), CryoSEM (c) and one 2D slice taken from XCT (d). Figure (a) and (c) are adapted from Metilli et al. (2021).

Polarized light microscopy (PLM) (Figure 2a) images allowed visualization the air bubbles and the birefringent fat crystals, which were found to stabilize the air-oil interface in oleofoams (Metilli et al., 2021). The fat crystals were clearly visible in the continuous phase and bridging neighbouring bubbles. Non-spherical air cells were detected, with diameters between 10 and 100 µm. However, estimating a size distribution of the air bubbles with this method was challenging, as air bubbles were subject to severe deformation and coalescence during sample preparation. Confocal microscopy images (Figure 2b) provided better-resolved air bubbles, which also appeared non-spherical. Information on the fat crystals was not available, as the

fluorescent dye stained both the oil and the fat crystals. Despite the ability of CSLM to provide stacks of images in the z direction, lengthy acquisition times and a smaller field of view (FoV) compared with tomography constituted a hindrance for measuring the bubbles' size and morphology, as the microscopy images might not be representative of the whole 3D sample. Micrographs collected with CryoSEM (Figure 2c) show a freshly cut surface from the bulk of the oleofoam, which is not accessible with other microscopy techniques. The higher resolution of this technique and the cryogenic conditions allowed to visualize the porous microstructure closer to its native state. Similarly to CSLM, the field of view of CryoSEM is limited compared with tomography techniques, and the sample preparation is also lengthier, not to mention the introduction of artefacts while imaging soft materials (Groves & Parker, 2013). Figure 2d shows a 2D tomography slice of an oleofoam sample, where the air bubbles appeared darker compared to the continuous oil phase. Clusters of brighter pixels were visible and, by comparison with Figure 2a, this suggested that XCT could locate the presence of fat crystals in oleofoams. However, further experiments with higher spatial resolution and improved contrast are required to confirm this hypothesis.

Comparison of different imaging protocols for SR-XCT

The first imaging protocol – room temperature, 10 ms exposure time, for a 20 seconds total acquisition time – allowed to reconstruct an acceptable tomogram, with most of the air bubbles having a defined boundary (Figure S1, Supporting Information 1). However, significant deformation on the edge of the sample occurred during stage rotation, as highlighted with red circles in Figure S1. In some instances, the deformation was excessive and prevented the reconstruction and the analysis of the 3D sample microstructure. Longer exposure times resulted in sample melting, again preventing reconstruction. Considering that CB oleofoams display a melting point between 25 and 27°C (Metilli et al., 2021), enhanced stabilization by cooling and controlling the sample temperature was sought to improve tomography acquisition procedure and the quality of the images.

Figure 3 shows a tomography slice of an oleofoam sample (15S) acquired using the second imaging protocol, *i.e.* sample cooling with liquid nitrogen, temperature control with the Cryojet and 100 ms exposure time.

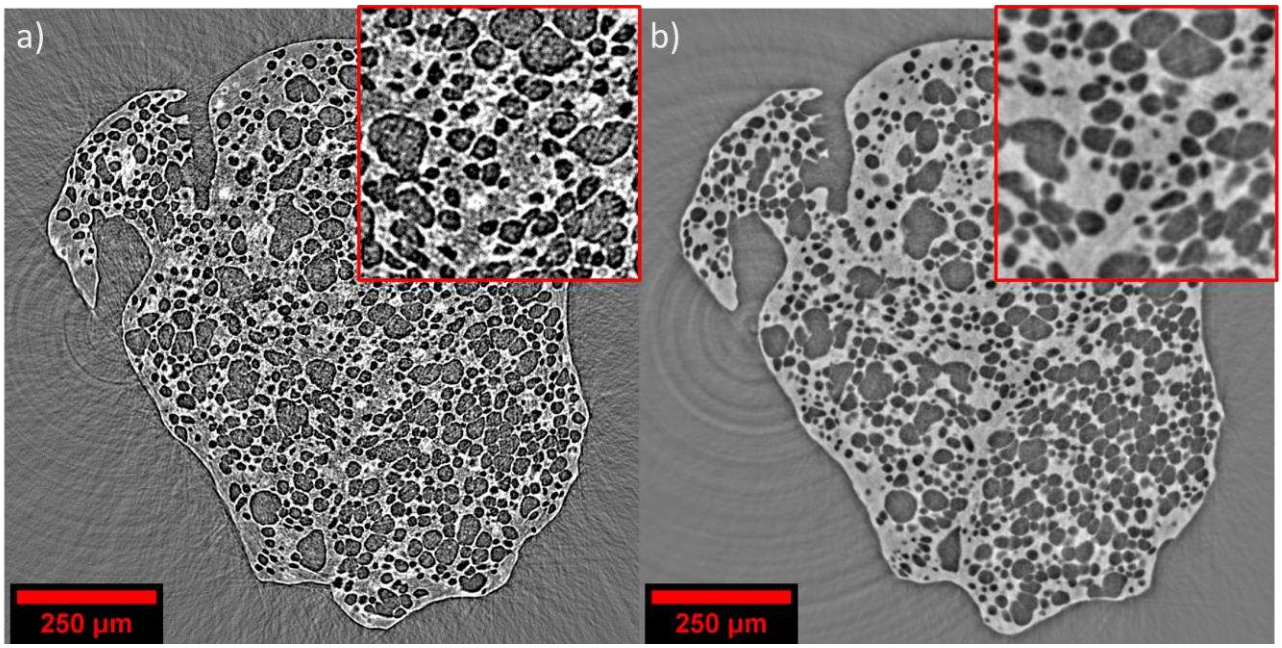

Figure 3. Tomography slice of a 15S oleofoam sample obtained with the second acquisition protocol (sample cooled with liquid nitrogen, maintained at -40°C and using 100 ms exposure time), reconstructed displaying the attenuation contrast (a). Same sample, displaying the phase-contrast mode (b). Zoomed areas showing crystal aggregates are displayed in the top right part of the image.

Because of the temperature control during the measurements and the cooling with liquid nitrogen applied to the samples prior the experiment, no deformation was detected in the reconstructed tomogram. To further improve the quality of the images, the phase-contrast mode, which is commonly used for weakly absorbing specimen in XCT, was applied during reconstruction (Nielsen et al., 2016; Guo et al., 2017; Wang et al., 2018). The Paganin-filtered image is shown in Figure 3b, displaying a more homogeneous pixel intensity across the image compared with the attenuation-contrast mode (Figure 3a). The phase imaging mode also resulted in a smoother contour for the brighter crystal aggregates visible in Figure 3a (insert, top right), leading to their pixel intensity being similar to the continuous phase and thus not distinguishable in the reconstructed image. Hence, the improved signal-to-noise ratio induced by the Paganin filter was beneficial for the characterization of the porous microstructure of the samples.

ImageJ Post-Processing

On closer inspection of Figure 4a, it can be seen that bright pixels were present inside air cells – especially larger ones – which was mostly caused by ring artefacts in the tomography reconstruction. Hence, a segmentation of the air phase based on the greyscale value alone was not feasible.

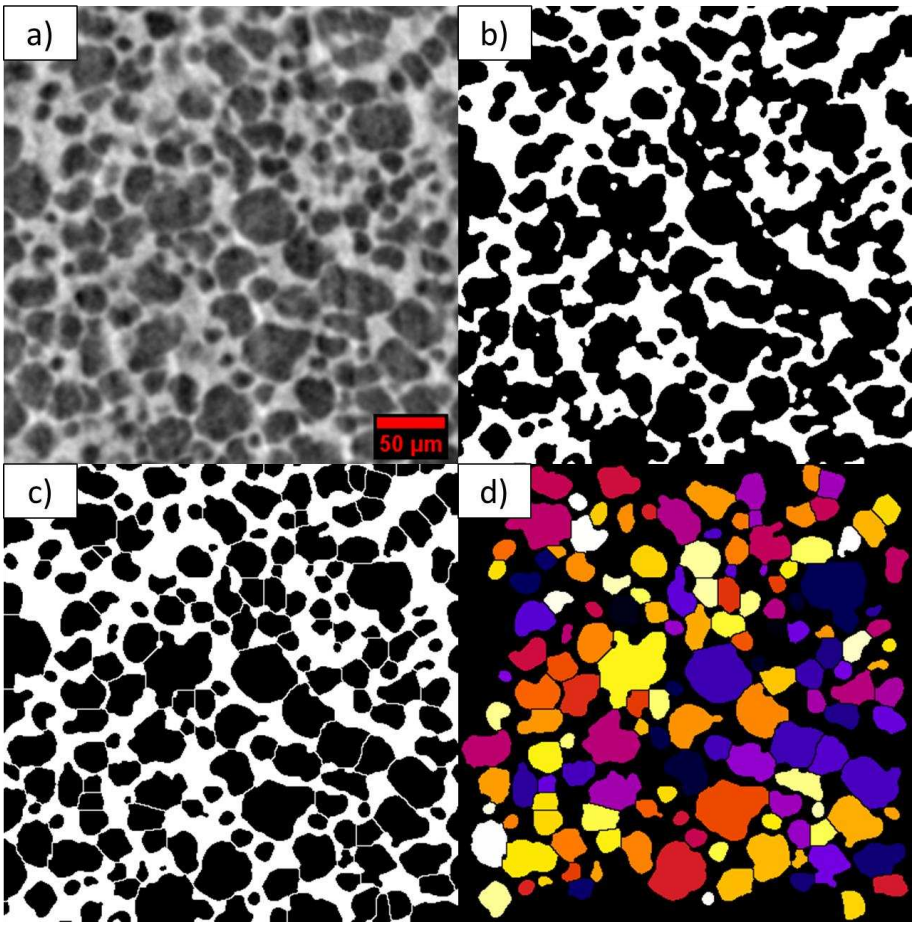

Figure 4. Image post-processing workflow developed in this methodology using ImageJ 1.53. Original reconstructed slice (a), binarized using Otsu threshold method (b), segmented with 3D Euclidean distance map watershed (c) and objects counted with the "Analyze Particles" function in BoneJ (d).

Therefore, an image post-processing workflow was then applied to enhance the quality of the images to separate the air bubbles from the continuous phase. Application of 3D median filter and thresholding resulted in a binarized image with several bubbles appearing connected (Figure 4b). The thresholding method chosen was based on the Otsu algorithm, which returns for each image a threshold value that maximizes inter-class variance; in other words, it divides the pixels into two classes, background and foreground (Russ, 2015). The validity of the method was assessed by visually comparing the thresholded images with the starting greyscale analogues. The watershed function based on the Euclidean Distance Map was then successfully applied to separate the connected air cells (Figure 4c). The counted objects in the slice are displayed in Figure 4d, which excluded air cells partially on the edge of the VOI, to avoid underestimation of the bubble size distribution. Recently, the use of machine learning-driven segmentation for image analysis has become popular, and may be considered a promising alternative to more traditional workflows.

However, it does require a set of synthetic images to train the algorithm, which implies prior knowledge of the sample microstructure (Ali et al., 2021).

Estimation of sample density

Tomography data were used to calculate the samples' bulk density and the values estimated were compared with the overrun values measured using the cup method described in the methodology section. Two oleofoam samples, 15S and 30F, were analysed after 5 minutes of aeration (Figure 5a and 5c), and after 30 minutes of aeration (Figure 5b and 5d). Table 1 contains the overrun of four individual VOI and its average, compared with the overrun measured experimentally.

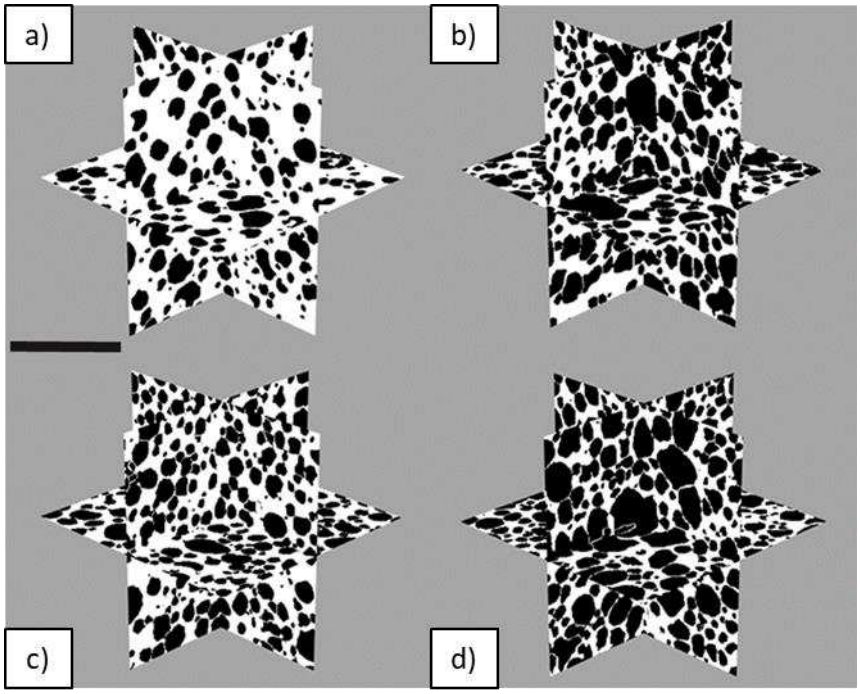

Figure 5. Orthogonal projections of selected VOI, obtained from ImageJ 3D viewer plugin, of samples 15S 5Min (a), 15S 30Min (b), 30F 5Min (c) and 30F 30Min (d). Scale bar represents 250 µm.

	15S 5 Minutes		15S 30 Minutes	
	Sample 1	Sample 2	Sample 1	Sample 2
VOI 1	76.3	87.1	131.3	137.1
VOI 2	78.8	139.0	119.9	146.3
VOI 3	71.0	95.5	109.2	185.7
VOI 4	70.9	115.9	138.0	216.8
OR % XCT	**73.7 ± 3.4[a]**	**118.7 ± 24.0[a]**	**125.9 ± 15.7[a]**	**171.2 ± 26.0[a]**

OR % Cup	76.3 ± 2.7[a]	75.0 ± 11.5[b]	183.7 ± 11.8[b]	196.7 ± 10.2[a]
	30F 5 Minutes		30F 30 Minutes	
	Sample 1	Sample 2	Sample 1	Sample 2
VOI 1	92.0	62.4	139.8	85.2
VOI 2	88.6	72.5	128.1	194.1
VOI 3	89.7	54.7	134.1	163.2
VOI 4	90.8	75.2	127.6	204.9
OR % XCT	**89.7 ± 1.9[a]**	**61.2 ± 11.3[a]**	**135.4 ± 6.6[a]**	**125.8 ± 31.9[a]**
OR % Cup	68.1 ± 19.4[b]	70.8 ± 6.4[a]	170.5 ± 17.3[b]	133.5 ± 16.2[a]

Table 1. Calculated overrun from SR-XCT data for individual VOI from selected oleofoam samples, their average and the respective overrun measured with the cup method. Values in the same column labelled with different letters have a statistically significant difference (p = 0.05).

The comparison of overrun estimation with the two different methods did not present a clear trend between the two techniques, for both 15S and 30F oleofoams, after 5 minutes of aeration. While for some samples the overrun measured with the cup method and SR-XCT were in agreement, in other repeats SR-XCT overestimated the overrun by 60% or 20% (see Table 1, 15S 5 minutes sample 2 and 30F 5 minutes sample 1). After 30 minutes of aeration, on the other hand, there was a consistent overestimation by the cup method of the overrun calculated by SR-XCT, for all samples. In particular, for sample 15S the overestimation was between 15% and 43%, whereas for sample 30F was between 6% and 26%. The differences in estimated density with the two techniques were most likely due to the difference in volume being analysed, 30 mL for the cup method and few cubic millimetres with SR-XCT. The overestimation by the cup method suggested the presence of larger voids in the sample, which might result from filling the cup during weighing, or being already present in the specimen, but remaining undetected by SR-XCT. Similarly, the presence of air bubbles of comparable size with the VOI resulted in overrun values with large standard deviation in several samples (Figure S2 in Supporting Information 2).

However, SR-XCT provides information on the distribution of the air bubbles and the homogeneity of overrun within samples that are not detectable with the cup measurement. From the observation of the different VOIs measured for each sample it is clear that sample 30F displayed, on average, more overrun homogeneity (smaller standard deviation) compared with sample 15S (larger standard deviation).

Density validation of XCT in bread dough research showed better agreement with gravimetric methods (Trinh et al., 2013; Koksel et al., 2016); however, it should be noted that the sampled XCT volume was in the magnitude of centimetres cube (as opposed to few millimetre cubes of this work) and that the method for measuring dough density involves fluid displacement (Campbell et al., 2001), which is may not be applicable to highly porous materials such as oleofoams. In other research fields, such as artificial bone scaffolds, cake filters and steel pipes corrosion, the density of porous matter measured by XCT is routinely validated by gas pycnometry or mercury injection porosimetry (Jones et al., 2007; Feng et al., 2020;; Wang et al., 2021). However, these techniques are destructive and might not be suitable for soft materials that do not possess a continuous pore network. The authors reported that differences in estimated density between porosimetry and XCT are affected by the resolution of the tomographic scanner, and by the choice of thresholding method. The air bubbles in oleofoams, in particular, usually cover the range between 10 and 100 µm in diameter (Fameau & Saint-Jalmes, 2020; Heymans et al., 2017), hence are likely to be detected by the current SR-XCT setup.

The effect of thresholding on the resulting overrun for oleofoams samples was also explored. The Huang and Wang (Huang & Wang, 1995) and Renyi's Entropy (Sahoo et al., 1997) methods were tested on sample 15S after 30 minutes of aeration, and compared with the default Otsu method used in this work (Table 1). The image segmentation and calculated overrun were similar between the Huang and Wang, and Otsu methods (134.7 ± 7.2 % vs. 152.3 ± 6.7), whereas the Renyi's Entropy produced binary images with excessive void compared with the greyscale 2D image, and very high overrun values (241.5 ± 33.2) (see Supporting Information 3, Table S1 and Figure S3). Therefore, the Otsu method was found to be the most reliable of the ones tested.

While the increase in overrun between 5 and 30 minutes of aeration was observed by both SR-XCT and the gravimetric method (*i.e.* the cup method), the latter technique provides a more reliable bulk density measurement due to the larger volume analysed. Nevertheless, SR-XCT provided essential information about the degree of aeration homogeneity in at the microscale, which directly affects the stability of the product during storage (Heymans et al., 2017; Fameau & Saint-Jalmes, 2020).

Effect of heating on oleofoam microstructure quantified by SR-XCT

After the image pre- and post-processing, SR-XCT data were used to estimate quantitative information about the air phase in oleofoams. Two samples with significantly different microstructure were analysed and compared. The first sample, 30F Fresh, was collected from the vessel after 30 minutes of aeration and imaged at -40°C with SR-XCT. The second sample, 30F Heated, was collected from the same batch of sample 30F Fresh, but was subjected to controlled heating, and then imaged with SR-XCT. The microstructure of the two samples is presented in Figure 6, as reconstructed tomographic slices.

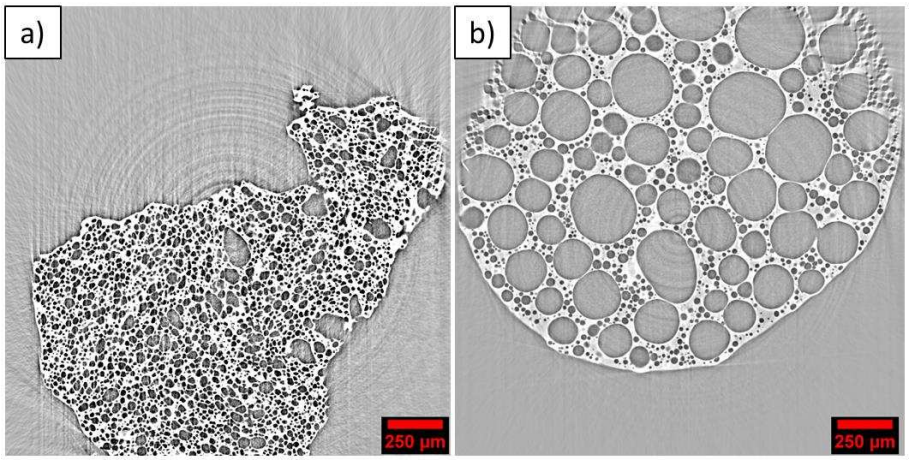

Figure 6. Tomographic slices of a fresh 30F oleofoam sample (a) and a 30F Heated sample (b), obtained after holding the sample at 300K (27°C) for 5 minutes.

The fresh sample (Figure 6a) contained mostly non-spherical small bubbles (average diameter < 50 µm), with few larger ones (diameter *ca.* 100 µm). The air phase was distributed homogeneously in the continuous oleogel phase, with domains containing both bubbles and a thin layer of oleogel in between. The heated sample (Figure 6b), on the other hand, presented fewer larger and rounder air bubbles, with diameters exceeding 300 µm, along with a population of smaller bubbles (average diameter < 50 µm). The oleogel phase comprised either very thin layers separating large bubbles, or areas where bubbles were not present at all.

406 The effect of heating on the microstructure of oleofoams was monitored with XRR, where 2D projections of
407 the sample from the side were collected during the temperature ramp.

408 The evolution of the microstructure of sample 30F Fresh to 30F Heated is shown in Figure 7.

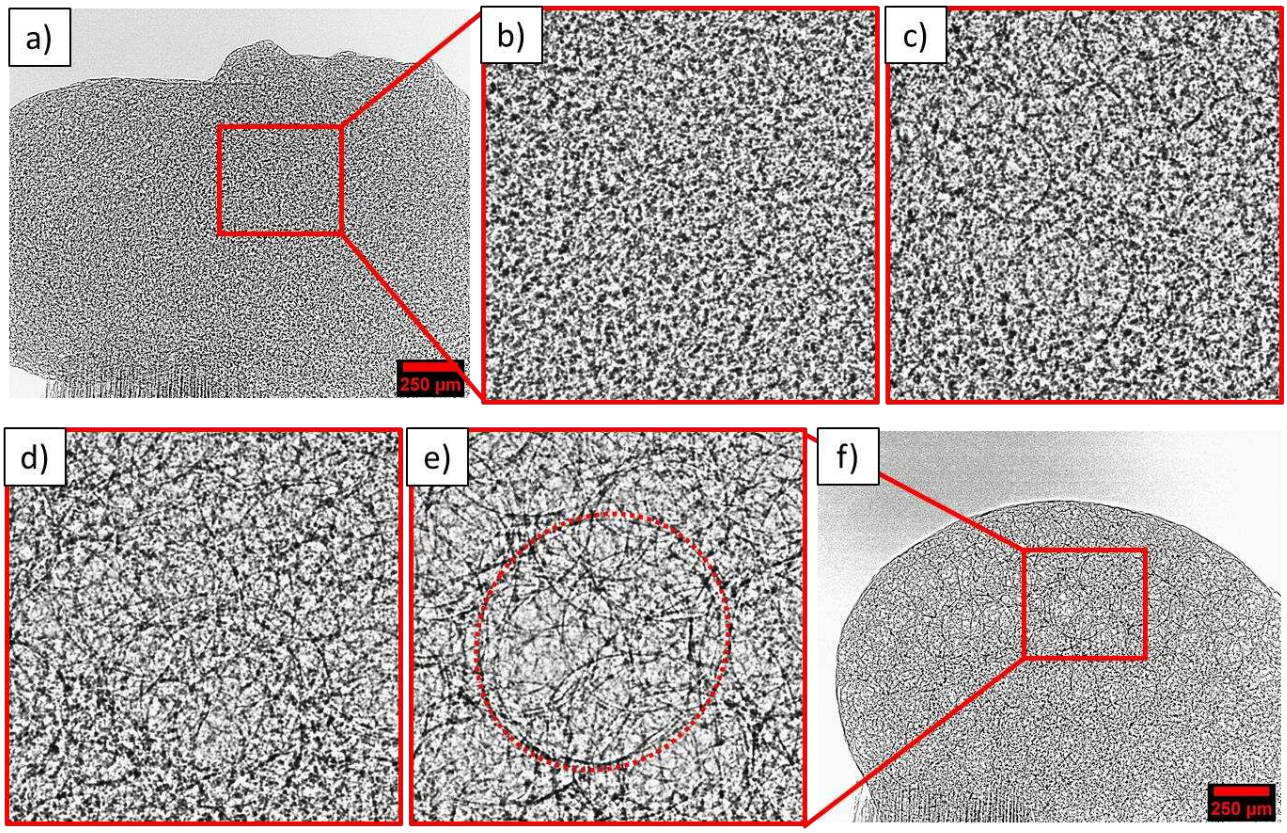

409

410 *Figure 7. XRR images of the 30F fresh oleofoam before heating (a) and at the end of the temperature ramp (f). Magnifications (b) to*
411 *(e) highlight the occurrence of a large air bubble during heating. Frame b) was taken after 7.21 minutes, c) after 8.29 minutes, d) after*
412 *8.45 minutes and e) after 12.37 minutes.*

413

414 By inspecting Figure 7a, the porous microstructure of the sample was not straightforward to resolve, as
415 multiple layers of air bubbles were overlaid in the 2D projections due to the large field of view. However,
416 with increasing temperature (from Figure 7b to 7e) larger bubbles, approximately 300 µm in diameter,
417 appeared, as a result of the heating step. Moreover, by comparison of Figure 7a and 7f, it can be noticed that
418 the whole sample partially collapsed to a rounder structure, owing to the partial melting of the fat network
419 in the continuous phase, as well as the rearrangement of the air bubbles driven by the surface tension forces
420 at the air-oil interface. In order to highlight the changes in the microstructure during heating, a stack of
421 difference images was calculated from the stack of radiography frames by subtracting the pixel values of the

i-th frame from the pixel values of the *i+1*-th frame. An example of processed image can be found in Figure S4 (Supporting Information 4), as well as the time-lapse sequence of the difference images (Figure S5, Supporting Information 5). From these images, it can be seen that the air bubbles were subject first to a rapid expansion (between one frame and the following, hence with a speed equal or faster to 0.667 seconds), followed by a slower expansion that lasted over several frames (hence seconds). In particular, the coalescence of two neighbouring air bubbles was captured during the experiment, showing that the newly-formed bubble relaxed "slowly" (*i.e.* over a few seconds in the following frames) to a slightly more spherical shape. Analysis of ten difference images containing the contours of different air bubbles revealed that, during heating, bubbles with an average equivalent diameter of 140.2 ± 35.2 µm and an average circularity of 0.94 ± 0.02 appeared in the oleofoam microstructure. The values are clearly an estimate, as some larger bubbles did not display a complete contour in the difference image to allow precise measurements of their size and shape, and smaller bubbles did not exhibit enough contrast to be detected. To further characterize the effects of heating on the sample, a principal component analysis (PCA) was performed on the stack of the difference images collected during the heating profile. the first principal component (PC) score was plotted against time and the temperature profile during heating (Figure S6, Supporting Information 6).

The PC score, which describes the changes in the pixel distribution in the stack of difference images, remained constant during most of heating ramp. A large variation in the PC score was observed in correspondence with the sample reaching 300 K (27 °C), which corresponded to the melting temperature of sample 30F. This variation reflected the occurrence of large air bubbles while the crystals melted, as the air phase was subject to coalescence without the stabilization of the Pickering crystals. Upon the start of the cooling ramp, the PC score returned to the baseline value with a steeper rate than the heating ramp, as the destabilisation of the foam microstructure was reduced at lower temperatures.

The microstructure characterization of some representative oleofoam samples is presented in Figure 8 - 10, displaying the three-dimensional rendering of a representative VOI each, the size distribution and the sphericity distribution, respectively. Table 2 contains the relevant parameters describing the size and shape of the air bubbles and the oleogel phase for each of the samples depicted in Figure 8.

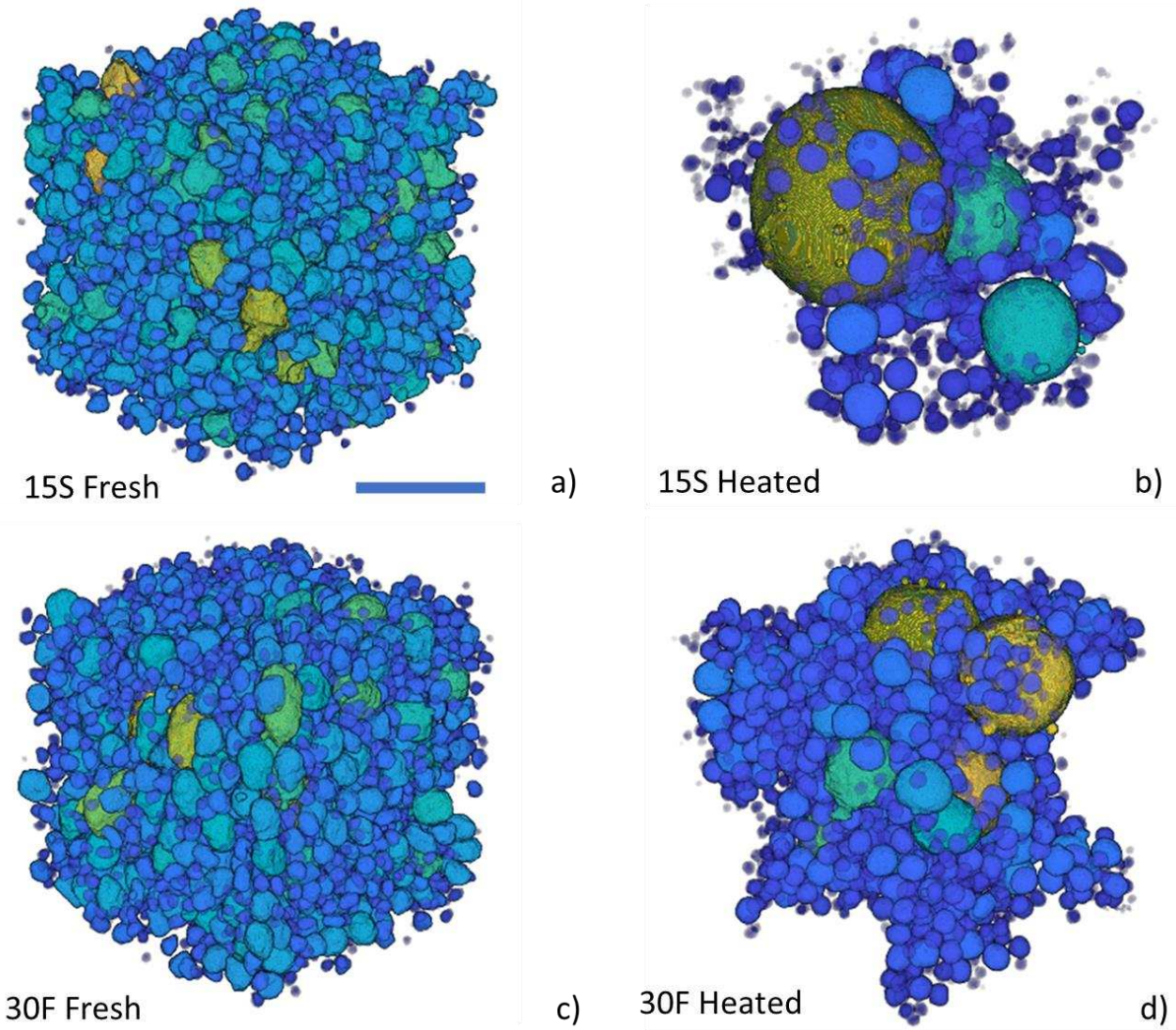

448

449

450 *Figure 8. 3D MATLAB renderings of selected VOIs of samples 15S Fresh (a), 15S Heated (b), 30F Fresh (c) and 30F Heated (d). The air*
451 *bubbles are colour-coded based on their equivalent diameter, from smallest (blue) to largest (dark yellow).*

452

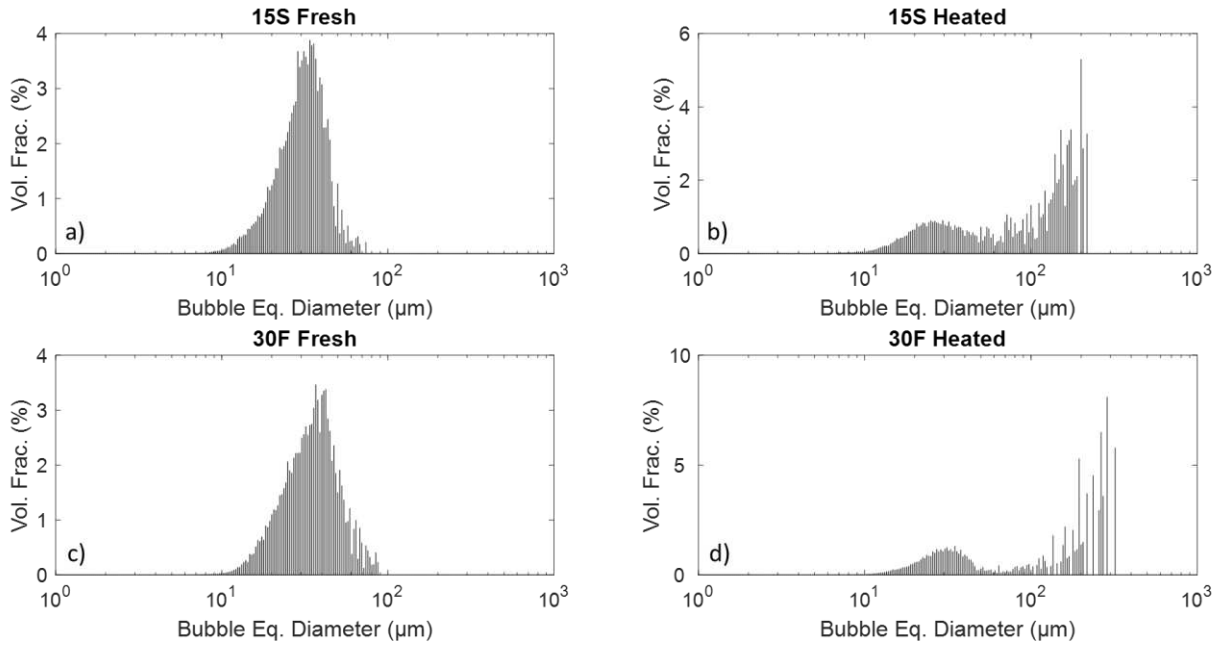

Figure 9. Air bubbles' size distribution for samples 15S Fresh (a), 15S Heated (b), 30F Fresh (c) and 30F Heated (d), calculated with MATLAB.

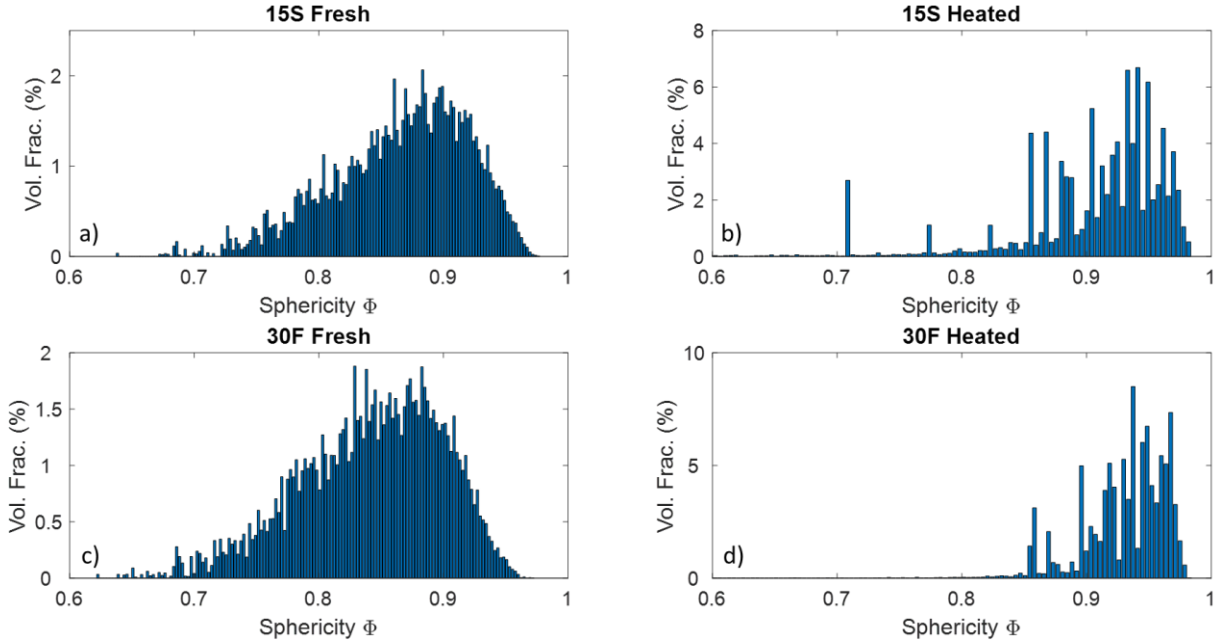

Figure 30. Air bubbles' sphericity distribution for samples 15S Fresh (a), 15S Heated (b), 30F Fresh (c) and 30F Heated (d), calculated with MATLAB.

Both fresh samples (15S and 30F) displayed a similar bell-shaped distribution, with an equivalent diameter of 32.10 ± 10.3 µm and 34.2 ± 14.1 µm, respectively (Figure 9a,c). This value was in agreement, for sample 30F, with the microstructure shown in Figure 6a. At the same time, the sphericity distribution of the two fresh samples were similar, ranging from 0.70 to 0.95, with a mean value of 0.91 ± 0.06 (15S Fresh) and 0.89 ± 0.06 (30F Fresh) (Figure 10a, c). This large distribution reflected the non-spherical shape of the air bubbles,

also visible in the volume rendering of Figure 8a and Figure 8c. For sample 30F Fresh, this was confirmed by the low volume fraction (44%) of spheroid-shaped bubbles; sample 15S Fresh, on the other hand, contained a higher amount of spheroid-shaped bubbles (75%) (See Supporting Information 7, Figure S7) (Table2).

Upon heating, both 15S and 30F samples displayed a significant change in their microstructure, exhibiting a bimodal size distribution with presence of two populations of bubbles: the first at *ca.* 27 µm for sample 15S and at *ca.* 32 µm for sample 30F, and the second with a maximum volume at *ca* 180 µm and *ca.* 287 µm, respectively (Figure 9b, d). In fact, the D[4,3] value for heated samples increased to 107.7 ± 67.1 µm (15S Heated) and 152.5 ± 106.3 µm (30F Heated), as the larger air bubbles contributed more significantly to the distribution. The average diameter for sample 30F was also close with the value obtained from the radiography images (140.2 ± 35.2 µm). The average sphericity increased for both samples, as well as the volume fraction of spheroidal bubbles; in particular, for sample 30F, the variation in the shape of the air bubbles was more significant (44% vs. 98%), in agreement with the observed relaxation of the air bubbles following the thermal treatment observed with XRR in Figure 7.

Furthermore, the normalized number density of bubbles decreased for both samples after heating: 47.1 ± 4.8 vs. 21.3 ± 3.0 for sample 15S and from 33.9 ± 1.9 to 13.6 ± 4.1 for sample 30F, explained by the occurrence of fewer, but larger bubbles due to coalescence after subjecting the sample to heating. This was visible also in Figure 6 by comparison of fresh and heated microstructure. The change in the microstructure was also reflected in the oleogel phase thickness, which increased from 11.5 ± 5.2 µm to 20.0 ± 9.9 µm (sample 15S) and from 8.8 ± 3.6 µm to 15.1 ± 5.8 µm (sample 30F). The change in the continuous gel phase was in agreement, for sample 30F, with the images in Figures 6a and 6b.

Table 2. Summary of the parameters describing the microstructure of sample 30F Fresh and 30F Heated, including the volume-weighted mean equivalent diameter (D[4,3]), the sphericity, volume fraction of spheroidal bubbles, number of bubbles per VOI, and mean oleogel thickness.

	15S Fresh	15S Heated	30F Fresh	30F Heated
D[4,3] (µm)	32.0 ± 10.3	107.7 ± 67.1	34.2 ± 14.1	152.5 ± 106.3
Sphericity	0.91 ± 0.06	0.93 0.06	0.89 ± 0.06	0.94 ± 0.04

Vol. % of spheroidal bubbles (%)	75.7	89.5	44.0	98.6
Number of bubbles / 10^6 * μm^3	47.1 ± 4.8	21.3 ± 3.0	33.9 ± 1.9	13.6 ± 4.1
Mean Oleogel Thickness (µm)	11.1 ± 5.2	20.0 ± 9.9	8.8 ± 3.6	15.1 ± 5.8

Conclusions

This work demonstrated the use of SR-XCT as a non-invasive technique for fast and accurate quantitative investigation of the microstructure of thermally sensitive, soft porous matter specimens prone to deformation with a straightforward, adaptable sample preparation and beamline setup. Sample stabilization by means of plunge-freezing with liquid nitrogen prior to XCT analysis, followed by the use of a Cryojet temperature control, enabled the collection of high-quality tomography data, suitable for the extraction of quantitative information. Using propagation based phase-contrast mode allows to achieve the image quality needed for segmentation without staining the samples with contrast agents. In particular, the phase-contrast mode was applied to improve the quality of the reconstructed images.

The overrun of the samples calculated with XCT was compared with gravimetric measurements, which highlighted the advantage of SR-XCT to study the aeration homogeneity of the specimen at the microscale. A custom image processing workflow was developed to extract relevant descriptors of the porous microstructure, such as bubble size distribution and morphology, together with the thickness of the continuous phase. Furthermore, the use of time-resolved X-ray radiography enabled to track changes in the microstructure of samples subject to external stimuli such as heating. While the method was demonstrated using edible oil-based foams, it is applicable to all porous soft matter that presents similar challenges in its characterization.

Supporting Information

Supporting information contain additional figures, a time-lapse video of the radiography experiment, as well as the scripts used in ImageJ and MATLAB for the current work.

Declaration of Interest

The authors declare that they have no known competing financial interests or personal relationships that could have appeared to influence the work reported in this paper.

Acknowledgments

The X-ray tomography and radiography data were collected during beamtime MT21081 and MG24233-1 at beamline I13-2, Diamond Light Source, Didcot (UK). The authors would like to acknowledge the Engineering and Physical Sciences Research Council funded Centre for Doctoral Training in Soft Matter and Functional Interfaces, grant ref. no. EP/L015536/1 as well as Nestlé PTC Confectionery (York, UK) for the financial and writing support.

References

Ali, S., Mayo, S., Gostar, A. K., Tennakoon, R., Bab-Hadiashar, A., Cann, T. M., … Favaro, J. (2021). Automatic segmentation for synchrotron-based imaging of porous bread dough using deep learning approach. *Journal of Synchrotron Radiation*, *28*, 566–575. https://doi.org/10.1107/S1600577521001314

Babin, P., Della Valle, G., Chiron, H., Cloetens, P., Hoszowska, J., Pernot, P., … Dendievel, R. (2006). Fast X-ray tomography analysis of bubble growth and foam setting during breadmaking. *Journal of Cereal Science*, *43*(3), 393–397. https://doi.org/10.1016/j.jcs.2005.12.002

Bahram-Parvar, M. (2015). A review of modern instrumental techniques for measurements of ice cream characteristics. *Food Chemistry*, *188*, 625–631. https://doi.org/10.1016/j.foodchem.2015.05.017

Barigou, M., & Douaire, M. (2013). *X-ray micro-computed tomography for resolving food microstructures*.

Food Microstructures: Microscopy, Measurement and Modelling. Woodhead Publishing Limited. https://doi.org/10.1533/9780857098894.1.246

Blott, S. J., & Pye, K. (2008). Particle shape : a review and new methods of characterization and classification, 31–63. https://doi.org/10.1111/j.1365-3091.2007.00892.x

Campbell, G. M., Herrero-Sanchez, R., Payo-Rodriguez, R., & Merchan, M. L. (2001). Measurement of dynamic dough density and effect of surfactants and flour type on aeration during mixing and gas retention during proofing. *Cereal Chemistry*, *78*(3), 272–277. https://doi.org/10.1094/CCHEM.2001.78.3.272

Ciurzyńska, A., & Lenart, A. (2016). Effect of the aerated structure on selected properties of freeze-dried hydrocolloid gels. *International Agrophysics*, *30*(1), 9–17. https://doi.org/10.1515/intag-2015-0067

Cornwell, P. A. (2018). A review of shampoo surfactant technology: consumer benefits, raw materials and recent developments. *International Journal of Cosmetic Science*, *40*(1), 16–30. https://doi.org/10.1111/ics.12439

Dittmann, J., Eggert, A., Lambertus, M., Dombrowski, J., Rack, A., & Zabler, S. (2016). Finding robust descriptive features for the characterization of the coarsening dynamics of three dimensional whey protein foams. *Journal of Colloid and Interface Science*, *467*, 148–157. https://doi.org/10.1016/j.jcis.2015.12.055

Doube, M., Klosowski, M. M., Arganda-Carreras, I., Cordelières, F. P., Dougherty, R. P., Jackson, J. S., … Shefelbine, S. J. (2010). BoneJ: Free and extensible bone image analysis in ImageJ. *Bone*, *47*(6), 1076–1079. https://doi.org/10.1016/j.bone.2010.08.023

Dowd, B. A., Campbell, G. H., Siddons, D. P., & Marr, R. B. (1999). Developments in synchrotron x-ray computed microtomography at the National Synchrotron Light Source. *Proc. SPIE. 3772, Developments in X-Ray Tomography II*, (July 1999).

Ellis, A. L., Norton, A. B., Mills, T. B., & Norton, I. T. (2017). Stabilisation of foams by agar gel particles. *Food*

551 *Hydrocolloids*, *73*, 222–228. https://doi.org/10.1016/j.foodhyd.2017.06.038

552 Fameau, A.-L., & Saint-Jalmes, A. (2020). Recent Advances in Understanding and Use of Oleofoams.
553 *Frontiers in Sustainable Food Systems*, *4*(August), 1–6. https://doi.org/10.3389/fsufs.2020.00110

554 Fameau, A. L., & Binks, B. P. (2021). Aqueous and Oil Foams Stabilized by Surfactant Crystals: New Concepts
555 and Perspectives. *Langmuir*, *37*(15), 4411–4418. https://doi.org/10.1021/acs.langmuir.1c00410

556 Fameau, A. L., & Fujii, S. (2020). Stimuli-responsive liquid foams: From design to applications. *Current*
557 *Opinion in Colloid and Interface Science*, *50*, 101380. https://doi.org/10.1016/j.cocis.2020.08.005

558 Feng, Z., Dong, X., Fan, Y., Li, H., Dong, Y., Ma, X., & Chen, R. (2020). Use of X-ray microtomography to
559 quantitatively characterize the pore structure of three-dimensional filter cakes. *Minerals Engineering*,
560 *152*(May 2019), 106275. https://doi.org/10.1016/j.mineng.2020.106275

561 Groves, K., & Parker, M. L. (2013). *Appendix: Electron microscopy: principles and applications to food*
562 *microstructures*. *Food Microstructures*. Woodhead Publishing Limited.
563 https://doi.org/10.1533/9780857098894.2.386

564 Guo, E., Kazantsev, D., Mo, J., Bent, J., Van Dalen, G., Schuetz, P., … Lee, P. D. (2018). Revealing the
565 microstructural stability of a three-phase soft solid (ice cream) by 4D synchrotron X-ray tomography.
566 *Journal of Food Engineering*, *237*(May), 204–214. https://doi.org/10.1016/j.jfoodeng.2018.05.027

567 Guo, E., Zeng, G., Kazantsev, D., Rockett, P., Bent, J., Kirkland, M., … Lee, P. D. (2017). Synchrotron X-ray
568 tomographic quantification of microstructural evolution in ice cream – a multi-phase soft solid. *RSC*
569 *Adv.*, *7*(25), 15561–15573. https://doi.org/10.1039/C7RA00642J

570 Gürsoy, D., De Carlo, F., Xiao, X., & Jacobsen, C. (2014). TomoPy: A framework for the analysis of
571 synchrotron tomographic data. *Journal of Synchrotron Radiation*, *21*(5), 1188–1193.
572 https://doi.org/10.1107/S1600577514013939

573 Herremans, E., Bongaers, E., Estrade, P., Gondek, E., Hertog, M., Jakubczyk, E., … Nicolaï, B. (2013).
574 Microstructure-texture relationships of aerated sugar gels: Novel measurement techniques for

575 analysis and control. *Innovative Food Science and Emerging Technologies*, *18*, 202–211.
576 https://doi.org/10.1016/j.ifset.2013.02.003

577 Heymans, R., Tavernier, I., Danthine, S., Rimaux, T., Van Meeren, P., & Dewettinck, K. (2018). Food-grade
578 monoglyceride oil foams: The effect of tempering on foamability, foam stability and rheological
579 properties. *Food and Function*, *9*(6), 3143–3154. https://doi.org/10.1039/c8fo00536b

580 Heymans, R., Tavernier, I., Dewettinck, K., & Van der Meeren, P. (2017). Crystal stabilization of edible oil
581 foams. *Trends in Food Science and Technology*, *69*, 13–24. https://doi.org/10.1016/j.tifs.2017.08.015

582 Hildebrand, T., & Rüegsegger, P. (1997). A new method for the model-independent assessment of thickness
583 in three-dimensional images. *Journal of Microscopy*, *185*(1), 67–75. https://doi.org/10.1046/j.1365-
584 2818.1997.1340694.x

585 Hill, C., & Eastoe, J. (2017). Foams: From nature to industry. *Advances in Colloid and Interface Science*,
586 *247*(October 2016), 496–513. https://doi.org/10.1016/j.cis.2017.05.013

587 Huang, L. K., & Wang, M. J. J. (1995). Image thresholding by minimizing the measures of fuzziness. *Pattern*
588 *Recognition*, *28*(1), 41–51. https://doi.org/10.1016/0031-3203(94)E0043-K

589 Hussain, M., Chen, D., Cheng, A., Wei, H., & Stanley, D. (2013). Change detection from remotely sensed
590 images: From pixel-based to object-based approaches. *ISPRS Journal of Photogrammetry and Remote*
591 *Sensing*, *80*, 91–106. https://doi.org/10.1016/j.isprsjprs.2013.03.006

592 Iftimi, L. D., Edinger, M., Bar-Shalom, D., Rantanen, J., & Genina, N. (2019). Edible solid foams as porous
593 substrates for inkjet-printable pharmaceuticals. *European Journal of Pharmaceutics and*
594 *Biopharmaceutics*, *136*(December 2018), 38–47. https://doi.org/10.1016/j.ejpb.2019.01.004

595 Jekle, M., & Becker, T. (2011). Dough microstructure: Novel analysis by quantification using confocal laser
596 scanning microscopy. *Food Research International*, *44*(4), 984–991.
597 https://doi.org/10.1016/j.foodres.2011.02.036

598 Jones, J. R., Poologasundarampillai, G., Atwood, R. C., Bernard, D., & Lee, P. D. (2007). Non-destructive

599 quantitative 3D analysis for the optimisation of tissue scaffolds. *Biomaterials*, *28*(7), 1404–1413.
600 https://doi.org/10.1016/j.biomaterials.2006.11.014

601 Kennedy, M. J., Conroy, M. W., Dougherty, J. A., Otto, N., Williams, B. A., & Fleming, J. W. (2015). Bubble
602 coarsening dynamics in fluorinated and non-fluorinated firefighting foams. *Colloids and Surfaces A:*
603 *Physicochemical and Engineering Aspects*, *470*, 268–279.
604 https://doi.org/10.1016/j.colsurfa.2015.01.062

605 Kinoshita, N., Sasaki, Y., Marukawa, E., Hirose, R., Sawada, S. ichi, Harada, H., & Akiyoshi, K. (2020).
606 Crosslinked nanogel-based porous hydrogel as a functional scaffold for tongue muscle regeneration.
607 *Journal of Biomaterials Science, Polymer Edition*, *31*(10), 1254–1271.
608 https://doi.org/10.1080/09205063.2020.1744246

609 Koksel, F., Aritan, S., Strybulevych, A., Page, J. H., & Scanlon, M. G. (2016). The bubble size distribution and
610 its evolution in non-yeasted wheat flour doughs investigated by synchrotron X-ray microtomography.
611 *Food Research International*. https://doi.org/10.1016/j.foodres.2015.12.005

612 Lazidis, A., de Almeida Parizotto, L., Spyropoulos, F., & Norton, I. T. (2017). Microstructural design of
613 aerated food systems by soft-solid materials. *Food Hydrocolloids*, *73*, 110–119.
614 https://doi.org/10.1016/j.foodhyd.2017.06.032

615 Legland, D., Arganda-Carreras, I., & Andrey, P. (2016). MorphoLibJ: Integrated library and plugins for
616 mathematical morphology with ImageJ. *Bioinformatics*, *32*(22), 3532–3534.
617 https://doi.org/10.1093/bioinformatics/btw413

618 Luengo, G. S., Fameau, A. L., Léonforte, F., & Greaves, A. J. (2021). Surface science of cosmetic substrates,
619 cleansing actives and formulations. *Advances in Colloid and Interface Science*, *290*.
620 https://doi.org/10.1016/j.cis.2021.102383

621 Manzocco, L., Mikkonen, K. S., & García-González, C. A. (2021). Aerogels as porous structures for food
622 applications: Smart ingredients and novel packaging materials. *Food Structure*, *28*(February).

https://doi.org/10.1016/j.foostr.2021.100188

Masselot, V., Bosc, V., & Benkhelifa, H. (2021). Analyzing the microstructure of a fresh sorbet with X-ray micro-computed tomography: Sampling, acquisition, and image processing. *Journal of Food Engineering*, *292*(July 2020), 2–10. https://doi.org/10.1016/j.jfoodeng.2020.110347

McClements, D. J. (2020). Future foods: A manifesto for research priorities in structural design of foods. *Food and Function*, *11*(3), 1933–1945. https://doi.org/10.1039/c9fo02076d

Metilli, L., Francis, M., Povey, M., Lazidis, A., Marty-Terrade, S., Ray, J., & Simone, E. (2020). Latest advances in imaging techniques for characterizing soft, multiphasic food materials. *Advances in Colloid and Interface Science*, *279*, 102154. https://doi.org/10.1016/j.cis.2020.102154

Metilli, L., Lazidis, A., Francis, M., Marty-terrade, S., Ray, J., & Simone, E. (2021). The Effect of Crystallization Conditions on the Structural Properties of Oleofoams Made of Cocoa Butter Crystals and High Oleic Sunflower Oil. *Crystal Growth and Design*. https://doi.org/10.1021/acs.cgd.0c01361

Mo, J., Guo, E., Graham McCartney, D., Eastwood, D. S., Bent, J., Van Dalen, G., … Lee, P. D. (2018). Time-resolved tomographic quantification of the microstructural evolution of ice cream. *Materials*, *11*(10), 1–14. https://doi.org/10.3390/ma11102031

Murray, B. S. (2020). Recent Developments in Food Foams. *Current Opinion in Colloid & Interface Science*, *50*, 101394. https://doi.org/10.1016/j.cocis.2020.101394

Murray, B. S., Durga, K., Yusoff, A., & Stoyanov, S. D. (2011). Stabilization of foams and emulsions by mixtures of surface active food-grade particles and proteins. *Food Hydrocolloids*, *25*(4), 627–638. https://doi.org/10.1016/j.foodhyd.2010.07.025

Nielsen, M. S., Munk, M. B., Diaz, A., Pedersen, E. B. L., Holler, M., Bruns, S., … Feidenhans'l, R. (2016). Ptychographic X-ray computed tomography of extended colloidal networks in food emulsions. *Food Structure*, *7*, 21–28. https://doi.org/10.1016/j.foostr.2016.01.001

Paganin, D., Mayo, S. C., Gureyev, T. E., Miller, P. R., & Wilkins, S. W. (2002). Simultaneous phase and

amplitude extraction from a single defocused image of a homogeneous object. *Journal of Microscopy*, *206*(1), 33–40. https://doi.org/10.1046/j.1365-2818.2002.01010.x

Pinzer, B. R., Medebach, A., Limbach, H. J., Dubois, C., Stampanoni, M., & Schneebeli, M. (2012). 3D-characterization of three-phase systems using X-ray tomography: Tracking the microstructural evolution in ice cream. *Soft Matter*, *8*(17), 4584–4594. https://doi.org/10.1039/c2sm00034b

Rau, C., Bodey, A. J., Marathe, S., Cipiccia, S., Zdora, M.-C., Zanette, I., … Storm, M. (2017). Micro- and nano-tomography at the DIAMOND beamline I13L imaging and coherence, (October 2017), 28. https://doi.org/10.1117/12.2274514

Russ, J. C. (2015). Image Analysis of Foods. *Journal of Food Science*, *80*(9), 1974–1987. https://doi.org/10.1111/1750-3841.12987

Saha, S., Saint-Michel, B., Leynes, V., Binks, B. P., & Garbin, V. (2020). Stability of bubbles in wax-based oleofoams: decoupling the effects of bulk oleogel rheology and interfacial rheology. *Rheologica Acta*, *59*(4), 255–266. https://doi.org/10.1007/s00397-020-01192-x

Sahoo, P., Wilkins, C., & Yeager, J. (1997). Threshold selection using Renyi's entropy. *Pattern Recognition*, *30*(1), 71–84. https://doi.org/10.1016/S0031-3203(96)00065-9

Sato, Y., Yamamoto, K., Horiguchi, S., Tahara, Y., Nakai, K., Kotani, S. ichiro, … Mazda, O. (2018). Nanogel tectonic porous 3D scaffold for direct reprogramming fibroblasts into osteoblasts and bone regeneration. *Scientific Reports*, *8*(1), 1–10. https://doi.org/10.1038/s41598-018-33892-z

Sehaqui, H., Salajková, M., Zhou, Q., & Berglund, L. A. (2010). Mechanical performance tailoring of tough ultra-high porosity foams prepared from cellulose i nanofiber suspensions. *Soft Matter*, *6*(8), 1824–1832. https://doi.org/10.1039/b927505c

Timounay, Y., Pitois, O., & Rouyer, F. (2017). Gas Marbles: Much Stronger than Liquid Marbles. *Physical Review Letters*, *118*(22). https://doi.org/10.1103/PhysRevLett.118.228001

Trinh, L., Lowe, T., Campbell, G. M., Withers, P. J., & Martin, P. J. (2013). Bread dough aeration dynamics

during pressure step-change mixing: Studies by X-ray tomography, dough density and population balance modelling. *Chemical Engineering Science*. https://doi.org/10.1016/j.ces.2013.06.053

Truong, T., Prakash, S., & Bhandari, B. (2019). Effects of crystallisation of native phytosterols and monoacylglycerols on foaming properties of whipped oleogels. *Food Chemistry*, *285*(January), 86–93. https://doi.org/10.1016/j.foodchem.2019.01.134

Turgay Celik. (2009). Unsupervised Change Detection in Satellite Images Using Principal Component Analysis and k-Means Clustering. *IEEE Geoscience and Remote Sensing Letters*, *6*(4), 772–776.

Ubbink, J., Burbidge, A., & Mezzenga, R. (2008). Food structure and functionality: a soft matter perspective. *Soft Matter*, *4*(6), 1569–1581. https://doi.org/10.1039/b800106e

Vo, T. N., Atwood, C. R., & Drakopoulos, M. (2018). Superior techniques for eliminating ring artifacts in X-ray micro-tomography. *Optics Express*, *26*(22), 28396–28412.

Wadeson, N., & Basham, M. (2016). Savu : A Python-based , MPI Framework for Simultaneous Processing of Multiple , N-dimensional , Large Tomography Datasets. *ArXiv*.

Wang, C., Hua, Y., Nadimi, S., Taleb, W., Barker, R., Li, Y., … Neville, A. (2021). Determination of thickness and air-void distribution within the iron carbonate layers using X-ray computed tomography. *Corrosion Science*, *179*, 109153. https://doi.org/10.1016/j.corsci.2020.109153

Wang, Z., Herremans, E., Janssen, S., Cantre, D., Verboven, P., & Nicolaï, B. (2018). Visualizing 3D Food Microstructure Using Tomographic Methods: Advantages and Disadvantages. *Annual Review of Food Science and Technology*, *9*(1), 323–343. https://doi.org/10.1146/annurev-food-030117-012639

Zhao, B., & Wang, J. (2016). 3D quantitative shape analysis on form, roundness, and compactness with μCT. *Powder Technology*, *291*, 262–275. https://doi.org/10.1016/j.powtec.2015.12.029